

# Multispectral to Hyperspectral using Pretrained Foundational model

Ruben Gonzalez\*<sup>1</sup>, Conrad M Albrecht<sup>1</sup>, Nassim Ait Ali Braham<sup>1</sup>,  
Devyani Lambhate\*<sup>2</sup>, Joao Lucas de Sousa Almeida<sup>2</sup>, Paolo  
Fraccaro<sup>2</sup>, Benedikt Blumenstiel<sup>2</sup>, Thomas Brunswiler<sup>2</sup>, and  
Ranjini Bangalore<sup>2</sup>

<sup>1</sup>Remote Sensing Technology Institute, German Aerospace Center  
(DLR), Germany

<sup>2</sup>IBM Research Labs, India, U.K., Zurich, Brazil

February 28, 2025

## Abstract

Hyperspectral imaging provides detailed spectral information, offering significant potential for monitoring greenhouse gases like CH<sub>4</sub> and NO<sub>2</sub>. However, its application is constrained by limited spatial coverage and infrequent revisit times. In contrast, multispectral imaging delivers broader spatial and temporal coverage but lacks the spectral granularity required for precise GHG detection. To address these challenges, this study proposes Spectral and Spatial-Spectral transformer models that reconstructs hyperspectral data from multispectral inputs. The models in this paper are pretrained on EnMAP and EMIT datasets and fine-tuned on spatio-temporally aligned (Sentinel-2, EnMAP) and (HLS-S30, EMIT) image pairs respectively. Our model has the potential to enhance atmospheric monitoring by combining the strengths of hyperspectral and multispectral imaging systems.

## 1 Introduction

Satellite images are being used to create detailed maps of Earth’s surface. These maps can be used for a variety of purposes, including navigation, urban planning, and environmental management. Recently there has been a surge in the launch of Hyperspectral satellites. Unlike multispectral satellites that capture a few broad bands, hyperspectral satellites capture hundreds of narrow bands, providing a much richer spectral fingerprint. Because of its ability to capture finer spectral information, it can be used for more precise applications like mineral mapping, greenhouse gases (GHGs) mapping, precision agriculture, surveillance,

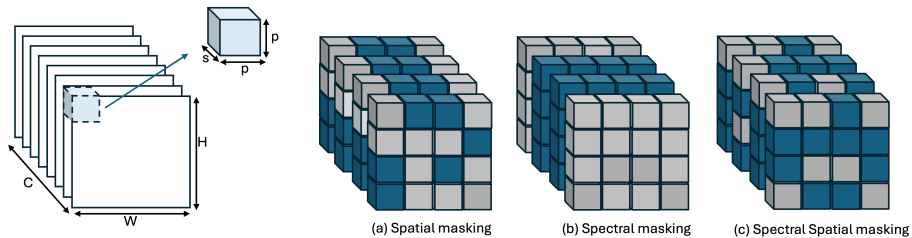


Figure 1: Masking strategies

water resource management, and many other tasks. Hyperspectral imaging has revolutionized many fields by enabling a detailed analysis of different matters and molecules based on spectral signatures. However, the revisit time of most of the hyperspectral satellites are much higher, which can be a limitation for time sensitive observations.

In contrast multispectral satellites have lower revisit time and broader spatial coverage. In this paper, we propose to generate Hyperspectral data from Multispectral data, for the periods when hyperspectral data is unavailable using foundational models.

Recently large-scale Image foundational models like Vision Transformer(ViT) [1], Stable Diffusion [2], and DALL-E [3] have revolutionized image generation, image classification and segmentation tasks. We have formulated the problem of generating hyperspectral data from multispectral data as a precise data generation case, where we want to generate all hyperspectral bands given the multispectral bands for a satellite Image using a ViT model. The ViT models focuses on capturing spatial relationships but lack the ability to capture spectral relationships. We therefore propose two modified version of vision transformers, specially adapted to capture the spectral and spatial-spectral relationships in the hyperspectral data.

We have performed two set of experiments to generate hyperspectral data from the multispectral data.

1. Multispectral data from Harmonized Landsat Sentinel-2 (HLS-S30) [4] is used to reconstruct the corresponding Earth Surface Mineral Dust Source Investigation (EMIT) [5] hyperspectral bands using a ViT-based model pre-trained on EMIT data.
2. Multispectral data from Sentinel-2 (S2) is used to reconstruct the corresponding Environmental Mapping and Analysis Program (EnMAP) [6] using a ViT-based model pre-trained on EnMAP data.

## 2 Related work

Spectral reconstruction bridges the gap between hyperspectral and multispectral imaging by enhancing spectral granularity. Early methods, such as dictionary-

based approaches [7] and Gaussian processes [8], relied on handcrafted priors but were limited in capturing non-linear spectral-spatial relationships. With the rise of deep learning, convolutional neural networks (CNNs) [9, 10] and attention-based transformers [11] have emerged as effective tools, leveraging data-driven learning to improve reconstruction accuracy. Recent approaches, such as hybrid attention networks [12], emphasize combining spatial and spectral attention for enhanced reconstruction quality.

Self-supervised learning (SSL) frameworks, like masked autoencoders (MAE) [13], naturally align with spectral reconstruction by leveraging large-scale unlabeled datasets to predict missing spectral information [14]. In hyperspectral remote sensing, studies such as [15] have demonstrated the effectiveness of self-supervised masked image reconstruction for adapting transformers to the unique characteristics of hyperspectral data. By integrating spatial-spectral self-attention, spectral positional embeddings, and blockwise patch embeddings, these models achieve significant accuracy improvements, particularly in label-scarce scenarios. Building on these insights, our work further explores spectral reconstruction with self-supervised transformers tailored for hyperspectral imagery.

## 3 Data

### 3.1 Pretraining datastes

**EMIT** uses an advanced imaging spectrometer instrument installed on the International Space Station that measures a spectrum for every point in the image. The EMIT data reflects the wavelengths from visible to short infrared wavelengths consisting 285 discrete bands, we have used 240 bands for our experiments with excluding the bands corresponding to water vapours and the first four bands. We use the Level 2A EMIT [16] product that contains the Surface reflectance derived by screening clouds and correction for atmospheric effects. The EMIT dataset used for Pretraining is split into 73,853 train, 4102 validation and 4102 test samples.

**EnMAP** is derived from two primary sources. HySpecNet-11k provides 11,483 hyperspectral images extracted from EnMAP tiles, covering wavelengths from 420 to 2,450 nm and comprising 202 usable spectral bands after atmospheric correction [17]. This dataset offers a manageable yet diverse subset of hyperspectral data for model training and evaluation. Complementing this, the SpectralEarth dataset comprises 538,974 hyperspectral images derived from EnMAP acquisitions between 2022 and 2024. With similar spatial and spectral characteristics to HySpecNet-11k, SpectralEarth provides extensive geographic and temporal coverage, making it well-suited for large-scale pre-training [18].

Masking	MSE			SSIM
	Train	Total	Unmasked	
Spec	7.11 E-4	9.17 E-4	9.25 E-5	0.7372
Spa-Spec	<b>4.27 E-4</b>	<b>5.6 E-4</b>	<b>2 E-5</b>	<b>0.8571</b>

Table 1: A comparison of Spectral (spec) and Spectral-Spectral (Spa-Spec) masking strategy with EMIT dataset. In these experiments, random 75% band groups are masked (similar to spectral masking) to evaluate the test set.

### 3.1.1 Finetuning Datasets

**HLS-S30 and EMIT** images from a harmonized surface reflectance product called HLS-2 (version 2.0) data are downloaded from NASA’s land processes distributed active archive center cumulus cloud as optimized GeoTIFFs. The Sentinel S30 data has been pre-processed to generate and select  $128 \times 128$  pixel<sup>2</sup> cloud-free patches. The data is processed to spatio-temporally align the EMIT and Sentinel-S30 pairs. This dataset is divided into 20691 train, 3205 validation, and 2190 test patches. Sentinel-S30 cloud-free patches with 13 channels were utilized to generate the corresponding 240 hyperspectral bands.

**S2 and EnMAP** The multispectral imagery is sourced from Sentinel-2, aligned spatially and temporally with the hyperspectral data of the HySpecNet-11k dataset. Level-2A-processed Sentinel-2 images were obtained via Google Earth Engine and matched to EnMAP acquisitions within a 3-day window to ensure comparable surface reflectance values. After cloud filtering, this mapping resulted in an 85.32% alignment between EnMAP patches and their corresponding Sentinel-2 images.

## 4 Pretraining Hyperspectral Foundational Model

### 4.1 Model Architecture

We used a very small version of the ViT model based on the MAE approach, a successful self-supervised learning method widely used and extended for different data types, including videos[19] and multispectral images [20]. The MAE reconstructs masked images using an asymmetric encoder-decoder architecture. The input image is divided into non-overlapping patches of the same size, and a subset of the patches is randomly masked. The encoder receives only the unmasked patches generating their latent representation. The decoder then receives the latent and masked tokens to perform the image reconstruction task [13].

We have 4 encoder and 2 decoder blocks in our very small ViT model. The number of heads are (8 and 8) and the embedding dimensions are (768 and 512), respectively, for (the encoder and the decoder). The images are  $128 \times 128 \times 240$  (H  $\times$  W  $\times$  C) dimensional. We have trained the model with a masking ratio (r) of 75%. Unlike the loss function used in ViT, which measures the

loss over just masked pixels, we use a holistic loss that measures the loss over the reconstruction of both masked and unmasked pixels. We have seen better convergence using the holistic loss function as compared to the loss over masked pixels.

## 4.2 Masking strategies

The ViT is pre-trained using a masking approach. We have explored two types of masking strategies in this paper: spectral and spatial-spectral. The input hyperspectral images has 3 dimensions, which are two spatial (H, W) dimensions and one spectral dimension (C), where C is the number of channels in the hyperspectral data. The spatial masking, where the input (H, W, C) is divided into patches of dimension (p, p, C) has proved to be very beneficial for several vision-based models as well as some remote sensing models. The problem with spatial masking is that it does not inherently capture spectral relationships. We therefore propose spectral and spectral-spatial masking for band reconstruction.

### 4.2.1 Spectral Masking

In Spectral masking strategy, the input (H, W, C) is divided into (p, p, s) patches with C/s band groups. Out of these C/s band groups, we randomly select r% of the band groups to be masked, where r is the masking ratio. If a band group is selected to be masked then all the spatial patches (p × p), corresponding to the selected band groups are masked. We have used band groups, instead of single bands here to take care of the increase in computational complexity if single bands were used.

### 4.2.2 Spatial-Spectral Masking

Similar to Spectral masking the input (H, W, C) is divided into (p, p, s) patches. And each of the patch of size (p × p × s) is either selected to be masked or unmasked randomly based on the masking ratio (r). The pictorial representation of all three masking strategies (spatial, spectral and spatial-spectral) are presented in the Figure 1.

## 5 Experiments and Results

### 5.1 Metrics

**MSE:** We have reported the Masked MSE (calculated only over masked pixels), Unmasked MSE (calculated only over unmasked pixels) and the total MSE.

**Structural Similarity Score (SSIM)** [21] : SSIM is a metric for evaluating the quality of digital images

$$\text{SSIM}(x, y) = \frac{(2\mu_x\mu_y + C_1)(2\sigma_{xy} + C_2)}{(\mu_x^2 + \mu_y^2 + C_1)(\sigma_x^2 + \sigma_y^2 + C_2)}$$

Where,  $x$  and  $y$  are the two images being compared,  $\mu_x$  and  $\mu_y$  are the mean intensities,  $\sigma_x^2$  and  $\sigma_y^2$  are the variances,  $C_1$  and  $C_2$  are the small constants to stabilize the division, for  $x$  and  $y$  respectively and  $\sigma_{xy}$  is the covariance of  $x$  and  $y$ .

## 5.2 A comparison of spectral and spatial-spectral pre-trained models

The spatial-spectral and spectral models are pre-trained on the EMIT dataset to get a comparison between the two masking techniques. The results are reported in Table 1. We notice that the model with spectral-spatial masking outperforms the model with spectral masking.

Dataset	Frozen/FT	Masking	MSE			SSIM
			Total	Masked	Unmasked	
HLS-S30-EMIT	Frozen	Spec	1.26 E-2	1.3 E-2	1.15 E-2	0.5366
HLS-S30-EMIT	FT	Spec	1.12 E-2	<b>1.14 E-2</b>	1.00 E-2	0.58
HLS-S30-EMIT	Frozen	Spa-Spec	<b>1.09 E-2</b>	<b>1.14 E-2</b>	<b>9.79E-3</b>	0.5908
HLS-S30-EMIT	FT	Spa-Spec	1.2 E-2	1.23 E-2	1.20 E-2	<b>0.7508</b>
Dataset	Frozen/FT	Masking	Total MSE			SSIM
S2-EnMAP	Frozen	Spec	9.96 E-3			0.582
S2-EnMAP	Finetuned	Spec	<b>3.89 E-3</b>			<b>0.767</b>

Table 2: Frozen and Finetuned model’s performance for HLS-S30 and EMIT dataset for Spectral (Spec) and Spatial-Spectral(Spa-Spec) masking

## 5.3 Reconstruction of Hyperspectral from Multispectral

After getting sufficient confidence in generating randomly masked EMIT bands, we tried to test the models for Multispectral to Hyperspectral conversion.

For this, we have aligned the Sentinel bands with the EMIT and EnMAP bands based on the frequencies (if there is more than 60% overlap between the frequencies, then we say there is a match). Wherever the match is found, bands are fixed to be the unmasked bands and the rest are the masked bands.

Table 2 summarizes the experiments for band reconstruction for the two data sets with and without fine-tuning. We have selected Frozen Spa-Spec model for the HLS-S30-EMIT dataset and Finetuned Spec model for the S2-EnMAP dataset to generate the plots in Figure 2 and 3 as they performed best with-respect-to the MSE metric. The frozen version have never seen any train samples of Sentinel data but still perform considerably well both in terms of MSE metric and reconstruction quality which can be seen from Figure 3-HLS-S30-EMIT plot. In all the spectral model versions, the results are further improved by fine-tuning. Whereas, with HLS-S30-EMIT dataset, we have seen an improvement only in the SSIM metric and not MSE for spatial-spectral

version. We have not included the results for spectral-spatial generation for the S2-EnMAP dataset as it is already covered in [15].

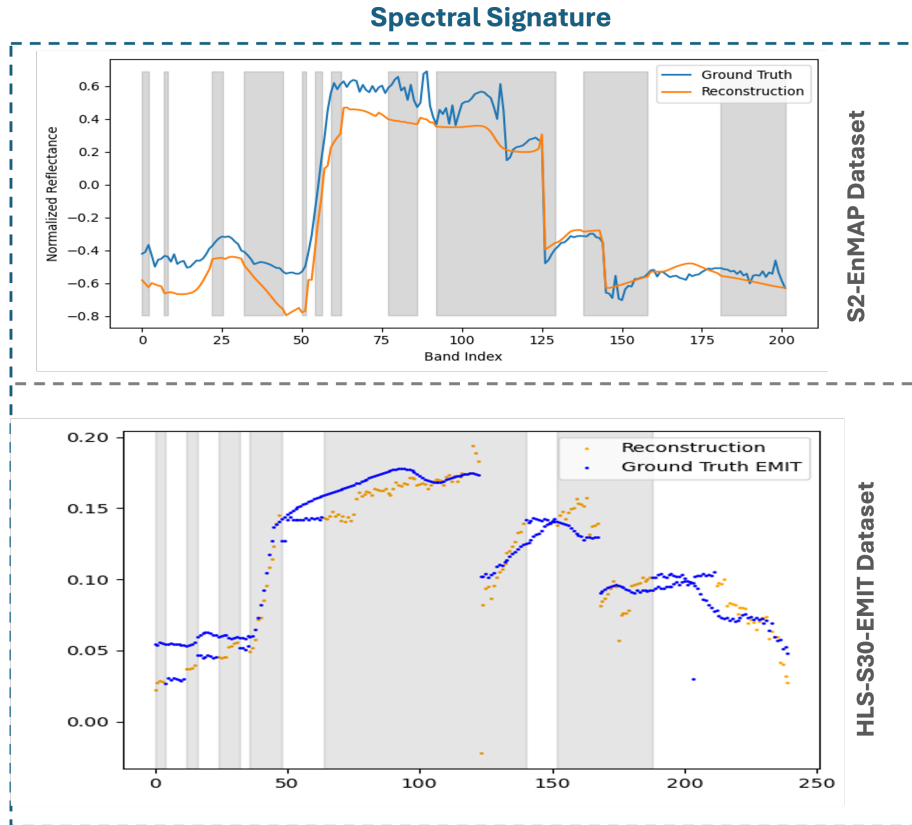


Figure 2: Spectral reconstruction for selected pixels for the two datasets. The masked bands are represented by Grey region and the unmasked bands are represented by White region.

## 6 Conclusion and Future Work

This study introduced the spectral and spatial-spectral transformer models for reconstructing hyperspectral data from limited spectral inputs, demonstrating accuracy and practical utility. The model effectively predicted missing spectral bands in masked hyperspectral data and enhanced spectral details when applied to multispectral inputs.

Our future plans include using the pre-trained models described in this paper for several downstream tasks like methane detection, CO<sub>2</sub> detection, Crop identification, Mineral classification, etc. We plan to further generalize the masking

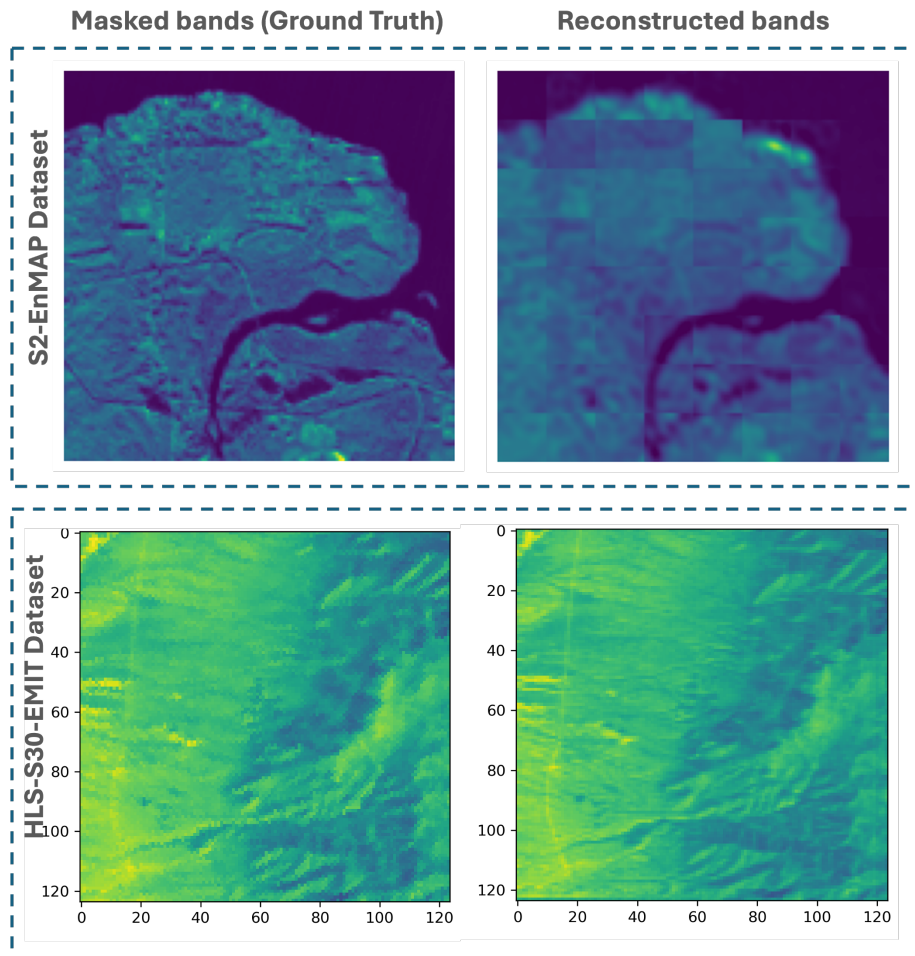


Figure 3: Original and reconstructed masked bands for the two datasets

approach by including a temporal dimension in the masking strategy. We also plan to work on multimodal models, which can process data from multiple hyperspectral/multispectral datasets.

## References

- [1] Gilad Sharir, Asaf Noy, and Lihi Zelnik-Manor, “An image is worth 16x16 words, what is a video worth?,” *arXiv preprint arXiv:2103.13915*, 2021.
- [2] Robin Rombach, Andreas Blattmann, Dominik Lorenz, Patrick Esser, and Björn Ommer, “High-resolution image synthesis with latent diffusion models,” 2021.



- [3] Aditya Ramesh, Mikhail Pavlov, Gabriel Goh, Scott Gray, Chelsea Voss, Alec Radford, Mark Chen, and Ilya Sutskever, “Zero-shot text-to-image generation,” 2021.
- [4] Martin Claverie, Junchang Ju, Jeffrey G. Masek, Jennifer L. Dungan, Eric F. Vermote, Jean-Claude Roger, Sergii V. Skakun, and Christopher Justice, “The harmonized landsat and sentinel-2 surface reflectance data set,” *Remote Sensing of Environment*, vol. 219, pp. 145–161, 2018.
- [5] “Data products,” <https://earth.jpl.nasa.gov/emit/data/data-products/>.
- [6] “Enmap,” <https://www.enmap.org/>.
- [7] Boaz Arad and Ohad Ben-Shahar, *Sparse Recovery of Hyperspectral Signal from Natural RGB Images*, 1 2016.
- [8] Naveed Akhtar and Ajmal Mian, “Hyperspectral Recovery from RGB Images using Gaussian Processes,” *IEEE Transactions on Pattern Analysis and Machine Intelligence*, vol. 42, no. 1, pp. 100–113, 10 2018.
- [9] Silvano Galliani, Charis Lanaras, Dimitrios Marmanis, Emmanuel Baltasvias, and Konrad Schindler, “Learned Spectral Super-Resolution,” *arXiv (Cornell University)*, 1 2017.
- [10] Zhiwei Xiong, Zhan Shi, Huiqun Li, Lizhi Wang, Dong Liu, and Feng Wu, “Hscnn: Cnn-based hyperspectral image recovery from spectrally under-sampled projections,” in *Proceedings of the IEEE International Conference on Computer Vision (ICCV) Workshops*, Oct 2017.
- [11] Yuanhao Cai, Jing Lin, Xiaowan Hu, Haoqian Wang, Xin Yuan, Yulun Zhang, Radu Timofte, and Luc Van Gool, “Mask-guided spectral-wise transformer for efficient hyperspectral image reconstruction,” *arXiv (Cornell University)*, 1 2021.
- [12] Xiangtao Zheng, Wenjing Chen, and Xiaoqiang Lu, “Spectral Super-Resolution of multispectral images using Spatial-Spectral Residual Attention Network,” *IEEE Transactions on Geoscience and Remote Sensing*, vol. 60, pp. 1–14, 8 2021.
- [13] Kaiming He, Xinlei Chen, Saining Xie, Yanghao Li, Piotr Dollár, and Ross Girshick, “Masked autoencoders are scalable vision learners,” in *Proceedings of the IEEE/CVF Conference on Computer Vision and Pattern Recognition*, 2022, pp. 16000–16009.
- [14] Jakob Hackstein, Gencer Sumbul, Kai Norman Clasen, and Begüm Demir, “Exploring masked autoencoders for sensor-agnostic image retrieval in remote sensing,” 2024.

- [15] Linus Scheibenreif, Michael Mommert, and Damian Borth, “Masked vision transformers for hyperspectral image classification,” in *2023 IEEE/CVF Conference on Computer Vision and Pattern Recognition Workshops (CVPRW)*, 2023, pp. 2166–2176.
- [16] DR Thompson, PG Brodrick, RO Green, O Kalashnikova, S Lundeen, G Okin, W Olson-Duvall, and T Painter, “Emit l2a algorithm: Surface reflectance and scene content masks—theoretical basis; earth mineral dust source investigation (emit),” *Jet Propulsion Laboratory, California Institute of Technology: Pasadena, CA, USA*, p. 23, 2020.
- [17] Martin Hermann Paul Fuchs and Begüm Demir, “Hyspecnet-11k: A large-scale hyperspectral dataset for benchmarking learning-based hyperspectral image compression methods,” 2023.
- [18] Nassim Ait Ali Braham, Conrad M Albrecht, Julien Mairal, Jocelyn Chanussot, Yi Wang, and Xiao Xiang Zhu, “Spectraearth: Training hyperspectral foundation models at scale,” 2024.
- [19] Zhan Tong, Yibing Song, Jue Wang, and Limin Wang, “Videomae: Masked autoencoders are data-efficient learners for self-supervised video pre-training,” *arXiv preprint arXiv:2203.12602*, 2022.
- [20] Yezhen Cong, Samar Khanna, Chenlin Meng, Patrick Liu, Erik Rozi, Yutong He, Marshall Burke, David Lobell, and Stefano Ermon, “Satmae: Pre-training transformers for temporal and multi-spectral satellite imagery,” *Advances in Neural Information Processing Systems*, vol. 35, pp. 197–211, 2022.
- [21] Zhou Wang, A.C. Bovik, H.R. Sheikh, and E.P. Simoncelli, “Image quality assessment: from error visibility to structural similarity,” *IEEE Transactions on Image Processing*, vol. 13, no. 4, pp. 600–612, 2004.